

Core Flow Modelling from Satellite-Derived ‘Virtual Observatories’

C.D. Beggan¹, K.A. Whaler¹ and S. Macmillan²

¹ *School of GeoSciences, University of Edinburgh, EH9 3JW, UK. Email: ciaran.beggan@ed.ac.uk*

² *British Geological Survey, Muchison House, Edinburgh, EH9 3LA, UK.*

5 August 2008

SUMMARY

Large satellite vector datasets of the Earth’s magnetic field have become available in recent years. Standard magnetic field models of the internal field are generated by parameterising a small subset of these data through a least-squares spherical harmonic representation. An alternative approach is to create a set of ‘virtual observatories’ (VO) in space, mimicking the operation of fixed ground-based observatories. We derive VO datasets from both CHAMP and Oersted satellite measurements using two different binning methods: (a) a grid of 648 VO cylinders of 400km radius, equally spaced at 10° in colatitude and longitude and (b) a global grid of 648 equal area tesserae. We use two different data selection techniques: (a) data from all local satellite times and (b) data from the local night-side only (20.00 - 06.00hrs). Corrections to the input data, using external and toroidal fields calculated by Comprehensive Model 4 (CM4), were also applied. In total, nine variations of VO datasets were formed. We calculate and directly invert the secular variation (SV) from these VO datasets, to infer flow along the core-mantle boundary. By examining the residuals from the flow models, we find temporally and spatially varying biases and patterns in the vector components. We investigate potential causes for these patterns and find evidence for influence from fields both internal and external to the satellite, orbital configuration and effects from the method of binning data. We conclude that the best fit of the flows to the data employs a grid of equal area tesserae using satellite

night-side only data. The use of CM4 to correct the satellite data before calculation of the VO grid removes a strong bias from external sources but, on average, does not greatly improve the fit of the flow to the data. We suggest that, despite best efforts, external fields effects are not completely removed from SV models and hence create unrealistic secular acceleration in the inverted flow models.

Key words: Core Flow Modelling – Geomagnetic Secular Variation – Magnetic satellite data

1 INTRODUCTION

The Earth's large scale magnetic field is believed to be generated and sustained by dynamo action within the fluid outer core. The main field changes in both strength and direction over time, with the gradual variation termed the secular variation (SV). With certain assumptions, it is conjectured that flow at the core-mantle boundary can be inferred (subject to some uncertainty) from the SV observed at, or above, the surface of the planet. Since the mid-nineteenth century, the strength and direction of the main field has been measured continuously at a limited number of fixed ground observatories, unevenly distributed across the globe (Bloxham et al., 1989). The last decade has seen a significant improvement in the capability to observe the global field at high spatial resolution. Several satellite missions have been launched, providing a rich new set of scalar and vector magnetic measurements from which to model the global field and temporal variation in detail. These new spatially comprehensive datasets complement the existing record of ground-based observatories. We exploit these new data to model the SV globally and attempt to improve upon the models of the core-boundary flow that have been constructed to date. We also use core flow modelling as a method to examine the effects of external field (and other influences) on models of the internal SV.

Using the approach developed by Mandaia & Olsen (2006), we create a set of 648 'Virtual Observatories' (VO), distributed about the planet at 400km above the Earth's surface, based upon satellite measurements from the CHAMP satellite (Reigber et al., 2002) and Oersted (Neubert et al., 2001) over five years (2001-2005). We invert the SV calculated at the VO for flow along the core-mantle boundary (CMB). Several previous studies have employed satellite data to recover

core flows (Hulot et al., 2002; Holme & Olsen, 2006) with recent results from Olsen & Mandaia (2008) suggesting that rapidly varying flows may occur within the core.

In contrast to most other studies, we invert SV directly from vector data – rather than spherical harmonic model coefficients – to calculate flow model coefficients, permitting the incorporation of data uncertainties into the model. Direct comparison of the SV generated by the flow model to the SV derived at individual VO can also be made, enabling the residuals to be investigated in detail. We analyse these results illustrating that it is difficult to produce a completely internal SV model.

Section 2 of this paper details the processing of satellite data to derive the VO, while Section 3 summarises the assumptions and method for flow inversion. In Section 4 we examine the patterns seen in the residuals between the SV produced by the flow model and the observed SV. We also simulate satellite data and invert the VO SV data derived from them for core flow. Section 5 assesses the evidence for potential causes and explanations for these residual patterns while Section 6 suggests methods for ameliorating the effects in the core flow models produced.

2 VIRTUAL OBSERVATORIES

Ground-based observatories provide a high-quality temporal record of the magnetic field at a single point on the surface of the Earth. Observations are taken typically at 1-second intervals, and made available in the form of minute, hourly, daily or monthly means. However, only a limited number of observatories are in simultaneous operation at any one time. The observatories are also unevenly distributed across the planet, with a large number concentrated in Europe and the Northern Hemisphere and a paucity in the Southern Hemisphere and Pacific Ocean region. Thus SV, as determined by ground observatories, is rather poorly constrained over large regions of the Earth.

Data from satellite missions (e.g. Magsat, Oersted, CHAMP, SAC-C) have the advantage of sampling the magnetic field across almost the entire globe. However, depending on the orbital configuration, the revisit period for any particular point may be several days to months. This gives a poor temporal record for any specific region and hence comparison directly to ground-based observatory records is difficult. Previous studies have overcome this issue by parameterising the field using a spherical harmonic representation and solving for a least-squares set of coefficients

which best fit the data (Hulot et al., 2002; Holme & Olsen, 2006). This approach generates a set of spherical harmonic coefficients representing both the field and the SV, though these field models are created from a very small selection of quiet-time data (Thomson & Lesur, 2007). The CHAOS field model (Olsen et al., 2006) contains a larger subset of slightly noisier quiet time data (Kp index ≤ 20) of satellite data from CHAMP, Oersted and SAC-C. However, this still represents a vast under-utilisation of the available data.

2.1 VO Method

Mandea & Olsen (2006) suggested another method for treating the large volumes of data generated during the satellite missions. By binning and averaging all available satellite vector data within a certain diameter of a selected point into monthly time periods, they were able to reproduce the change in the magnetic field as recorded at ground observatories. As this approach attempts to mirror the method used for deriving monthly mean values for ground-based observatories, they refer to these points above the surface of the planet as ‘virtual observatories’. A strong implicit assumption is that short-term external field effects will have a zero mean value over the period of a month.

To calculate the mean monthly field at a VO, the data must be reduced to a common height (due to the slightly elliptical and slowly decaying orbit of the satellite). Mandea & Olsen (2006) chose to bin data from a particular month are within cylinder of radius 400km about the chosen latitude and longitude of the VO position. A main field model (represented by three vector components, North (X), East (Y) and Downward (Z)) is subtracted from observed vector satellite data (\mathbf{B}):

$$\Delta\mathbf{B} = \mathbf{B}^{Satellite} - \mathbf{B}^{MainField} \quad (1)$$

to produce a set of residual measurements $\Delta\mathbf{B}$. It is assumed that the field can be represented as a Laplacian potential field $\Delta\mathbf{B} = -\nabla V$, which varies linearly in local x , y and z Cartesian coordinates, with the origin in the centre of the cylinder (at 400km altitude). This allows V to be calculated using 8 independent parameters:

$$V = v_x x + v_y y + v_z z$$

$$\begin{aligned}
& +v_{xx}x^2 + v_{yy}y^2 - (v_{xx} + v_{yy})z^2 \\
& +v_{xy}xy + v_{xz}xz + v_{yz}yz
\end{aligned} \tag{2}$$

These parameters $(v_x, v_y, \dots, v_{yz})$ are estimated using a Huber Robust Least-Squares method. The mean residuals to the main field at the virtual observatory are $\Delta\mathbf{B} = -(v_x, v_y, v_z)$. The main field model is added back to the residuals to produce values of the X , Y and Z components of the field for a selected month. This procedure is repeated for all the available months in the dataset at all VO locations.

The SV (or yearly change) at a given observatory for $month(t)$ is the difference between the average field in $month(t-6)$ and $month(t+6)$ for the North (X), East (Y) and Downward (Z) components.

$$SV_{month}(t) = Field_{month}(t+6) - Field_{month}(t-6) \tag{3}$$

This approach removes both the crustal field component of the signal and the annual variation, without any direct filtering or averaging, giving the \dot{X} , \dot{Y} and \dot{Z} vector components of the field.

In their study, Manda & Olsen (2006) found a strong correlation (for the period 2001.5-2005.5) between the SV observed at the Niemgk Observatory and the corresponding point at a height 400km above Niemgk in the \dot{X} and \dot{Z} components (though no strong correlation was present in the \dot{Y} component). Comparison of the SV at Niemgk and 21 other observatories to their respective ‘virtual observatory’ values gave a mean correlation of $|\rho| = 0.65, 0.21, 0.73$ for the \dot{X} , \dot{Y} and \dot{Z} components, respectively.

Initially, for this study, corrected and calibrated CHAMP vector data were acquired from GFZ Postdam (Level 2, Release v50) for the time period from May 2001 to December 2005 (56 months). Magnetic field series for 648 virtual observatories were calculated on two separate grids: (1) a regular grid of colatitude and longitude ($\theta = 5^\circ, 15^\circ, \dots, 175^\circ$; $\phi = -180^\circ, -170^\circ, \dots, 170^\circ$) mimicking the grid point arrangement of Manda & Olsen (2006) and (2) an equal area global grid of 648 tesserae (Leopardi, 2006). At higher latitudes on the grid of equal latitude and longitude, data included in the VO cylinders are binned into more than one VO, as the areas overlap. At lower latitudes, there are gaps between the cylinders, meaning some data are unused. Using a

grid of adjacent non-overlapping equal-area tesserae uses each measured datum just once in the calculation of the VO grid.

The CHAMP satellite samples the field at a frequency of 1Hz, giving over 86,000 points per day on average. The CHAOS model was used in Equation (1) as the main field model to compute the magnetic residuals. The parameters of Equation (2), were calculated by the Huber Robust Least-Squares algorithm. The 44 months of SV data and their standard deviations, from November 2001 to June 2005, were then estimated using 3.

3 FLOW MODELLING

Roberts and Scott (1965) examined the problem of determining the fluid motions at the core-mantle boundary responsible for SV, with Kahle *et al.* (1967) producing an initial computed solution. However, many assumptions must be made to formulate the problem and reduce ambiguities in the resulting solutions. Deducing the flow velocity from SV is non-unique, even with perfect knowledge of the observed radial part of the field (B_r) and the SV (\dot{B}_r), as there are entire classes of flow which do not generate any detectable SV outside the core (Backus, 1968).

3.1 Assumptions

Typically, the magnetic field lines are assumed fixed or ‘frozen’ relative to the core fluid motion over short periods of time (i.e. years to decades). This is known as the frozen-flux assumption (Alfvén, 1942). On large scales ($> 1000\text{km}$), the magnetic diffusion (due to Ohmic decay) can be argued to operate on timescales on the order of 2×10^5 years, so can be ignored on timescales from years to decades. There are shortcomings to this approach which are discussed, for example, in Gubbins & Kelly (1996) and Love (1999). Backus (1968) devised a test of the frozen flux assumption but from examination of data from recent satellite missions, Holme & Olsen (2006) have suggested that it may not be possible to conduct the test conclusively.

Further assumptions must be made to produce a tractable problem. In particular, in most cases, the flow is truncated at a large spatial scale and *a priori* constraints are imposed, giving a regularised solution via a damping (smoothing) parameter. Assumptions about the type of flow at the

core-mantle boundary (CMB) are also required to reduce the inherent ambiguity. Examples include steady (Voorhies & Backus, 1985), toroidal-only (Whaler, 1980) or tangentially geostrophic (Hills, 1979; Le Mouél, 1984) flows, or with a particular helicity (Amit & Olson, 2004). There are limits to the fidelity of the inverted flow models compared to the actual flows that generate the observed SV. A number of workers including Rau *et al.* (2000) and Amit *et al.* (2007) have inverted artificial SV data generated from dynamo simulations to test how well flow inversion recovered the actual velocities and patterns. Their work suggests that it is possible to image correctly only the large spatial scale parts of the flow. However, despite the numerous shortcomings of the methods and data, consistent flow model solutions (using large scale assumptions) are achieved from different datasets. In this sense, it may be possible to recover some aspects of the large scale flow within the outer core.

3.2 One-Norm Iterative Inversion

The inversion of observed SV data for a core flow model is undertaken with the use of a spectral spherical harmonic representation for the Main Field, SV, and the flow coefficients (Roberts & Scott, 1965; Whaler, 2007). The flow model vector \mathbf{m} can be expressed in terms of the poloidal and toroidal scalars, s and t , constructed from a spherical harmonic representation in a spherical polar coordinate system (r, θ, ϕ) (Bloxham, 1989). To solve for \mathbf{m} from the VO SV, a regularised inversion approach imposing large scale assumptions is employed. The two-norm (for Gaussian distributed uncertainties) form of the solution (Gubbins, 1983):

$$\hat{\mathbf{m}} = (\mathbf{A}^T \mathbf{E}^{-1} \mathbf{A} + \lambda \mathbf{D})^{-1} \mathbf{A}^T \mathbf{E}^{-1} \mathbf{d} \quad (4)$$

where \mathbf{A} is the matrix of normal equations, formed through the calculation of the Gaunt and Elsasser matrices, whose elements are derived from the main field spherical harmonic coefficients and the spatial derivatives of the input data positions (Whaler, 1986). \mathbf{E} is the data covariance matrix and \mathbf{d} is the data vector. \mathbf{D} is the regularisation matrix which can be used to incorporate *a priori* constraints, imposing a ‘smoothness’ (forcing the solution to be large scale) on the flow. Including \mathbf{D} into the formulation is equivalent to minimising a linear combination of the misfit norm and an initially defined solution norm. A damping parameter, λ , acts as to control the importance

attached to the data versus the imposition of a smooth flow. Regularisation also ensures numerical stability of the inversion and convergence of the expansion when the spherical harmonic series for \mathbf{m} is truncated.

This approach provides adequate results. However, Walker & Jackson (2000) provide the motivation to compute flow models using an iterative one-norm minimisation method instead, as it is observed that the residual fit of the SV generated by flow models to the data is generally Laplacian distributed. The residual differences from the previous iteration are used to form a diagonal matrix \mathbf{R} , whose elements are $R_{ii} = \sqrt{2}/|e_i|$, where e_i is the residual of the i th datum at the k th iteration. \mathbf{R} is re-calculated at each iteration. The iterative one-norm solution can be written as:

$$\hat{\mathbf{m}}_{k+1} = (\mathbf{A}^T \mathbf{E}^T \mathbf{R} \mathbf{E} \mathbf{A} + \lambda \mathbf{D})^{-1} (\mathbf{A}^T \mathbf{E}^T \mathbf{R} \mathbf{E} \mathbf{d}) \quad (5)$$

We apply the ‘strong norm’ of Bloxham (1988) as the *a priori* constraint in \mathbf{D} . This minimises a global measure of the flow complexity (where u is the flow vector, ∇_h is the horizontal divergence and l is the degree of truncation of the flow in the inversion):

$$\begin{aligned} \mathbf{m}^T \mathbf{Q} \mathbf{m} &= \oint_{CMB} [(\nabla_h^2 u_\theta)^2 + (\nabla_h^2 u_\phi)^2] dS \\ &= 4\pi \sum_l \frac{[l(l+1)]^3}{2l+1} \sum_{m=0}^l [(t_l^m)^2 + (s_l^m)^2] \end{aligned} \quad (6)$$

In this case, \mathbf{D} is diagonal with elements $l(l+3)^3/(2l+1)$. A geostrophic flow constraint can be applied as an additional physical constraint on the flow (Jackson, 1997). We have found that the use of iterative one-norm method greatly improves the fit of the model to the data compared to the two-norm, justifying the use of the Laplacian approach (Beggan & Whaler, 2008).

The CHAOS field model provides the main field coefficients for the Gaunt and Elsasser matrices (\mathbf{A} in Equation 5). The standard deviation of the residual misfit from the Huber Robust Least Square estimate of data fit to the VO field in $month(t-6)$ and $month(t+6)$ is used to form the data covariance matrix. The residual errors for the first iteration of the one-norm solution are obtained from an initial starting model calculated by a two-norm solution from the input data. The final solution of the one-norm iterative algorithm typically converges within 15-20 iterations.

We solve for flow coefficients up to degree and order $l = 14$. The value of very small ($< 10^{-4}$) error residuals in the matrix \mathbf{R} are set to 10^{-4} to prevent the formation of ill-conditioned matrices, as advocated by Walker & Jackson (2000). The damping parameter (λ) was set to 10^{-3} for all solutions.

The resulting flow model is forward modelled to produce the predicted SV at each VO. The residual at the i th VO is to $(d_i - \sum_j A_{ij}\hat{m}_j)$. Plotting the histogram of the residuals reveals how well fit the predicted SV generated by the flow model is to input SV from the VO. A perfect fit of the model to the data would produce a histogram with a single peak at zero.

4 BIASED RESIDUALS

Following the example of Manda & Olsen (2006) and Olsen & Manda (2007), we exploited all the available CHAMP vector data from *all* local times over each month to generate the global set of VO. Each cylindrical VO ‘bin’ (or tessera) contained a large number (250 to 10000) of points, depending on the data availability per month and generally increasing as a function of higher latitude (due to the polar orbit). Thus, the resulting monthly field model might reasonably be regarded as a confident estimate of the true field. Using Equation (3) to calculate the SV, we inverted the dataset to derive a flow model for each month. The residuals were expected to reveal a random pattern of positive and negative errors across the globe, but surprisingly, the residuals revealed biases, patterns and correlations between the \dot{X} , \dot{Y} and \dot{Z} components. In general, histograms of the residuals have a Laplacian distribution. However, the distribution of the residuals in each component reveals more complex spatial patterns, with strong temporal variation.

Figure 1 shows examples of the instantaneous flow, associated residual histogram and residual pattern for three separate months (from the equal latitude/longitude VO grid): Nov 2001, February 2003 and March 2005. In Figure 1 (a–c) the core flow models derived from the SV show large differences in flow patterns, and are evidently influenced by a temporally-changing signal in addition to the internal SV. The typical Southern Indian ocean gyre is present in all models, however, differences occur in the Northern hemisphere and under Western Eurasia. In Model B, a clockwise

gyre is present while in Models A and C, flow is reversed. These month-to-month change in flow are too large to be physically realistic.

The histograms of the residual fit of the SV generated by the flow model to the input data are shown in (d–f). The plots reveal a deviation from the best-fit Laplacian distributions. An unbiased dataset and flow inversion would be expected to produce an approximately zero-mean distribution of residuals. However, Model B has a significant negative skew with, arguably, a bimodal distribution (i.e. second peak at $-6nT/yr$). Model C has the smallest skew of the three histograms, but has a larger non-zero mean than Model A, suggesting that some bias still exists.

The geographical distribution of the residuals in the \dot{X} , \dot{Y} and \dot{Z} components are shown in (g–i). Examination of the distribution in each component of the SV suggests that the \dot{X} component is consistently the noisiest, whilst the \dot{Z} component tends to have the smallest residuals. The residuals in the \dot{X} component tend to be strongly biased – either positive or negative, while the \dot{Y} and \dot{Z} components have residuals with the opposite sign to \dot{X} (i.e. inversely correlated). In general, the component biases balance to generate an approximately zero-mean Laplacian distribution histogram. For some months, hemispherical biases are evident, and often longitudinal ‘bands’ or ‘stripes’ of larger (or alternating sign) residuals occur (e.g. the \dot{Y} components of Figure 1 (g) and (h)). If viewed as a time-series, the longitudinal stripes can be seen to ‘drift’ or rotate consistently westward by approximately $30^\circ/\text{month}$, matching the satellite orbital drift.

Figure 2 shows examples of flow models from VO calculated using a grid of equal area tesserae. The flow models in (a–c) are similar to Figure 1 indicating that the SV data from both gridding approaches are equivalent. The fit of the flow models to the data is slightly poorer, in these examples (compare the histograms (d–f) in Figures 1 and 2). The residual distribution (g–i) shows that the \dot{X} component is still the noisiest. The \dot{X} residuals in Figure 2(h) reveal that the bias is strongest in mid-latitudes, with opposite signed residuals in either hemisphere of the \dot{Z} component. The sectorial banding seen in the residual distributions (e.g. Figure 1(g) \dot{X}) is less apparent. The polar regions are less noisy, presumably due to fewer points in these regions. However, using the equal area tesserae grid improves the residual fit in $\approx 60\%$ of the months, reduces the sectorial

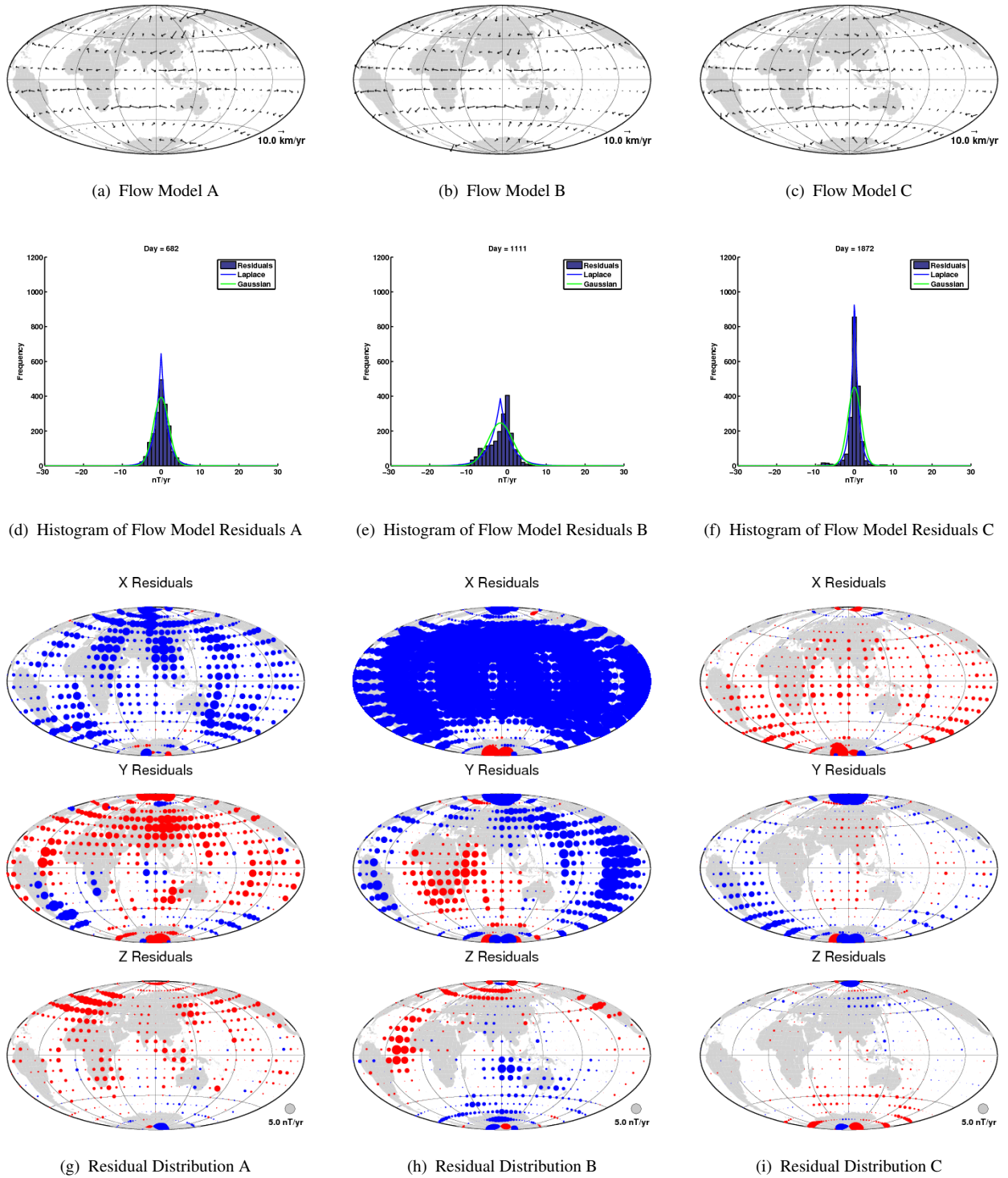


Figure 1. Core-mantle boundary flow models, (a–c), histograms (d–f) and geographic distribution (g–i) of the residual fit of each flow model to the SV generated from Virtual Observatory grid of equal latitude and longitude spacing for *all* available vector measurements. Model A: November 2001; Model B: February 2003; Model C: March 2005. In (d–f), the Laplacian and Gaussian fit to the data are shown in the blue and green curves respectively. In (g–i) circle size indicates residual size, with reference circle shown in bottom right. Positive residuals in red, negative residuals in blue. Continents shown for reference.

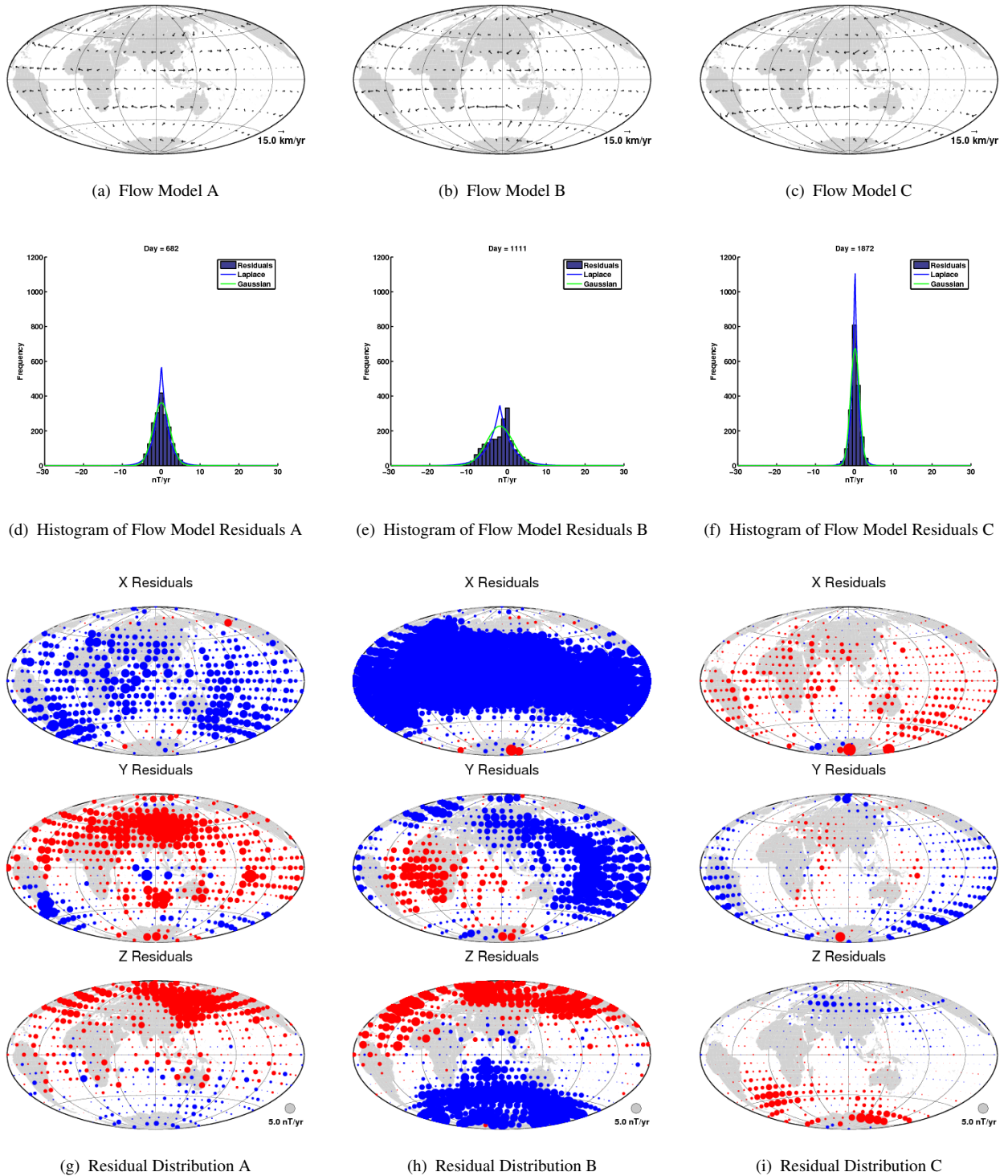


Figure 2. Core-mantle boundary flow models (a–c), histograms (d–f) and geographic distribution (g–i) of the residual fit of each flow model to the SV generated from Virtual Observatory data grid of equal area tessera for *all* available vector measurements. Model A: November 2001; Model B: February 2003; Model C: March 2005. In (d–f), the Laplacian and Gaussian fit to the data are shown in the blue and green curves respectively. In (g–i) circle size indicates residual size, with reference circle shown in bottom right. Positive residuals in red, negative residuals in blue. Continents shown for reference.

banding and skew of the histogram distribution, though the \dot{Z} residual component is, in general, noisier.

We wish to investigate if the residual bias results primarily from external or internal signals, orbital drift or other effects. A second set of main field VO for the period May 2001 – December 2005 were calculated using local *night-side only* satellite data. The CHAMP vector data were winnowed to remove measurements outwith the local time window of 20.00–06.00hrs (polar summer daylight conditions were ignored). The number of data in each cylindrical ‘bin’ (or tessera) was smaller (again dependent on the data availability during the particular month and latitude). Each month, approximately 5% of the VO did not have enough data to calculate a solution, so were spatially interpolated to fill the grid. As before, the SV for each VO was calculated and inverted for flow models for each month. We shall refer to this as VO Dataset 2, with the previous VO model using data from *all* local times called Dataset 1. Comparison of residual histograms from this dataset to those from Dataset 1 indicate that the fit of the flow model to the SV data has improved slightly. As for Dataset 1, flows from the grid of equal latitude/longitude better fit the data than those from the equal area tesserae grid. Figure 3 shows three examples of the geographic residual patterns using the equally spaced latitude/longitude grid. The \dot{X} , \dot{Y} and \dot{Z} components are still strongly biased, with the longitudinal stripes particularly evident in Figure 3 (b). Note that the residuals for these flow models are smaller than those for Dataset 1 (e.g. compare Figure 1(h) and 3(b)).

To examine the effects of external field influence in the residual biases and orbital influence in the sectorial banding, a dataset of selected quiet-time data from Thomson & Lesur (2007) was used to generate a third VO dataset (referred to as Dataset 3). The selection consists of vector data from both the CHAMP and Oersted satellites for the same time period (2001.4-2006), though due to the rigorous noise criteria imposed has very few data points (approximately 85000) compared to the previous CHAMP datasets. It was necessary to interpolate both spatially and temporally where lack of data prevented the calculation of an acceptable VO point. With such strong selection criteria, there should be little temporal correlation in the data. Comparisons do show that the SV calculated from this dataset is reasonably consistent with the other two datasets. The SV was again

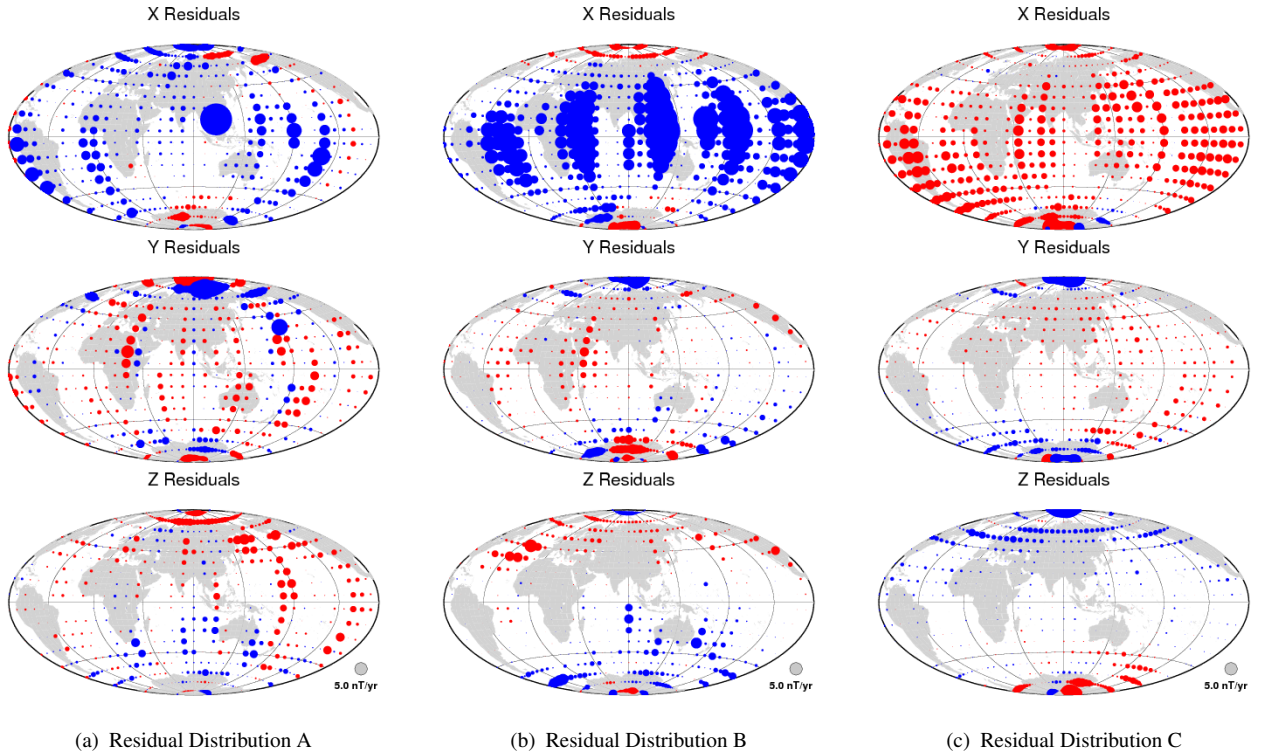


Figure 3. Geographic distribution of the residual fit of each flow model to the SV generated from Virtual Observatory grid of equal latitude and longitude spacing for *night-side only* vector measurements. Model A: November 2001; Model B: February 2003; Model C: March 2005. Circle size indicates residual size, with reference circle shown in bottom right. Positive residuals in red, negative residuals in blue. Positive residuals in red, negative residuals in blue. Continents shown for reference.

inverted to produce instantaneous monthly flow models, similar to those from previous datasets. Figure 4 shows examples of the resulting residual patterns. Few data were available for the end of the dataset, which resulted in poorer fit to the flows in the latter months. There is no obvious banding or strong bias in any of the components, suggesting that external noise may affect the residuals.

As a test of orbital configuration influence (for the sectorial banding pattern, in particular), a synthetic VO dataset was created using a simple satellite orbit simulator and the internal part of the CHAOS field model. Two years of synthetic satellite measurements and positions were simulated by combining the CHAOS model and the latitude, longitude and radius output from the satellite simulation. The data were binned into 400km cylinders on a regular grid of latitude and longitude to produce VO (similar to Figure 1) providing twelve months of SV values which were inverted for core flow models. A number of simple but unrealistic noise scenarios were tested using the

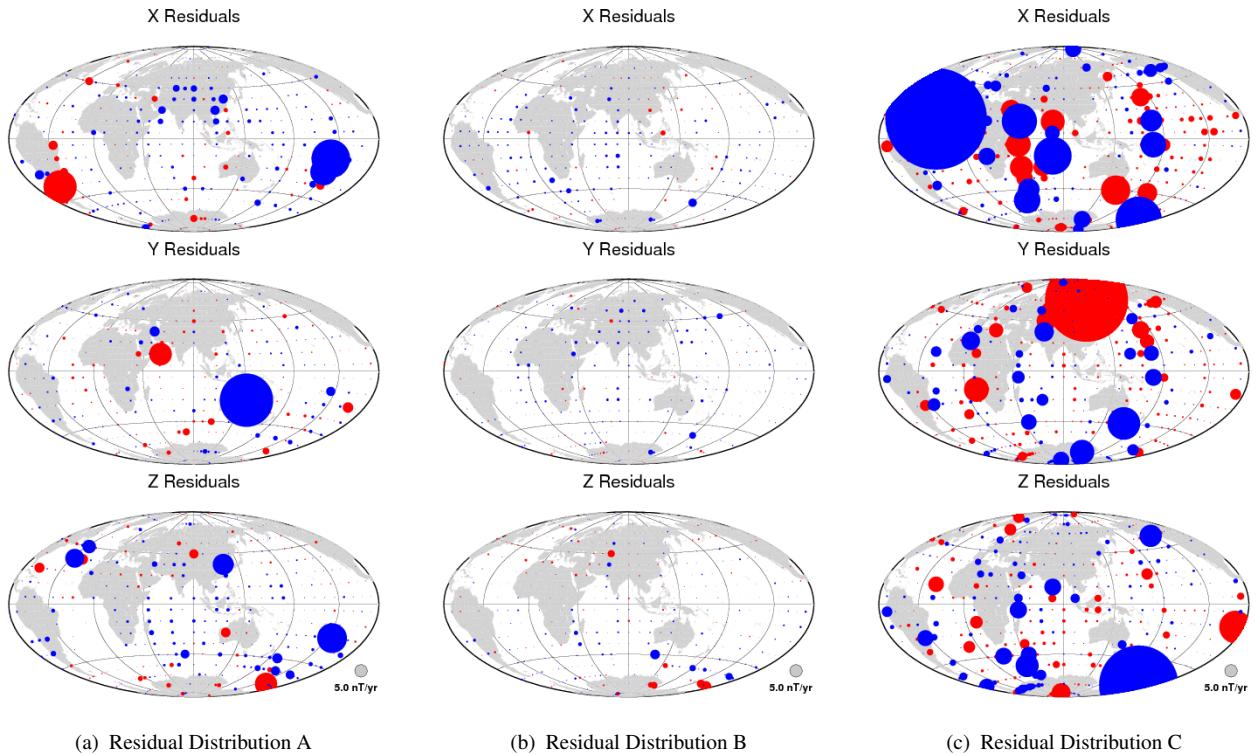


Figure 4. Geographic distribution of the residual fit of each flow model to the SV generated from Virtual Observatory grid of equal latitude and longitude spacing for *selected quiet-time* vector measurements. Model A: November 2001; Model B: February 2003; Model C: March 2005. Circle size indicates residual size, with reference circle shown in bottom right. Positive residuals in red, negative residuals in blue. Continents shown for reference.

simulation. Both biased (e.g. positive only) and unbiased random Gaussian noise was added to the CHAOS model in the polar regions and on the local dayside at low to mid latitudes, leaving other regions noise-free. Differing noise levels (up to $\sigma \leq 10nT$) have little effect on the size of the residuals and the pattern seen. Figure 5 shows residual distributions for three consecutive months from the noise-free VO simulation. The residuals are seen to have persistent longitudinal banding features which drift westward when viewed as a time series. This result demonstrates that the combination of binning approach and orbital drift is at least partly responsible for the sectorial banding of the residuals.

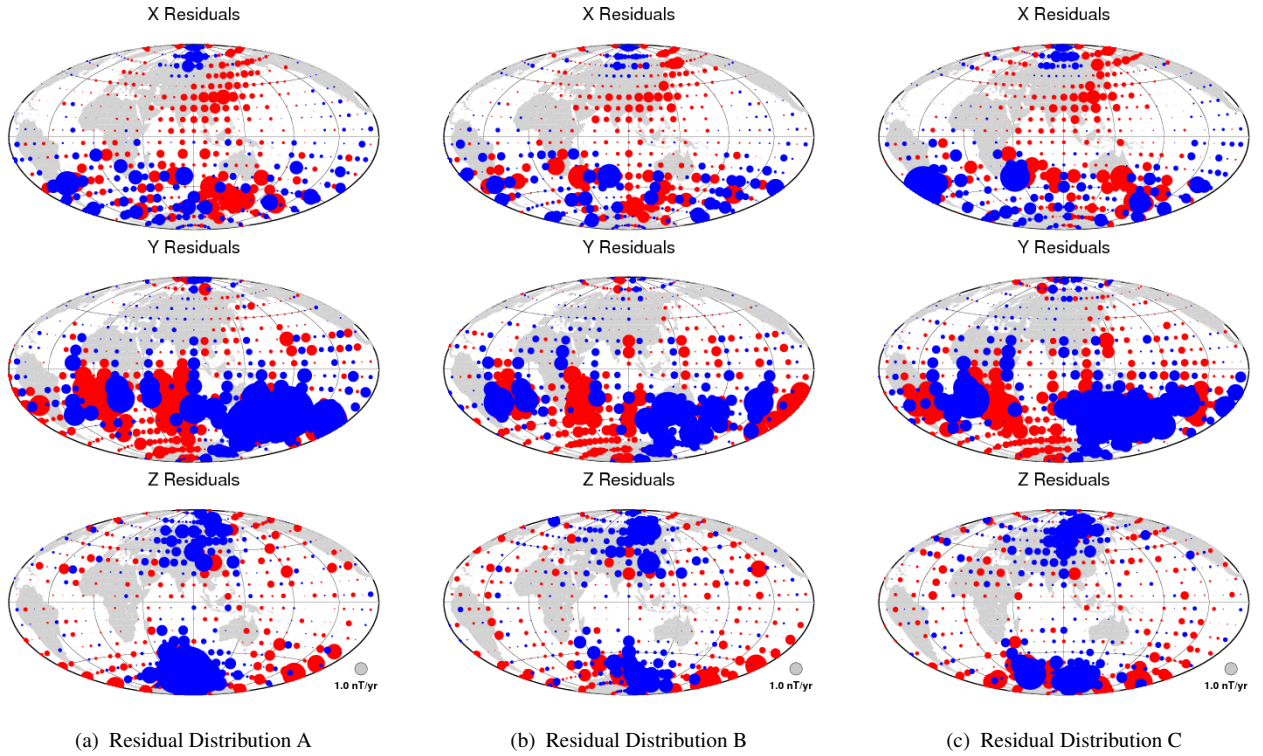


Figure 5. Geographic distribution of the residual fit of three flow models to SV data simulated from the CHAOS model and the CHAMP orbits generated from Virtual Observatory grid of equal latitude and longitude. Positive residuals in red, negative residuals in blue. Continents shown for reference.

5 ANALYSIS

It is worth emphasising that, in this study, core flow modelling is being employed as a method to study the consistency of the internal SV model, with the main aim being to understanding and remove undesired effects. Analysis of the patterns in the residuals allows correction strategies to be developed.

Previous studies employing direct inversion of SV data from ground based observatories have not reported strong geographically biased vector components (e.g. Beggan & Whaler, 2008), so it is of interest to attempt to identify potential influences for the component biases and patterns seen, particularly the deviation from the implicit assumption of zero-meant noise. There are several suggested causes for the strong biases seen in Dataset 1 and Dataset 2. These include effects from (a) fields external to the satellite orbit, (b) fields internal to the satellite orbit, (c) the orbital configuration of the satellite and (d) the method of binning and preparing the SV datasets.

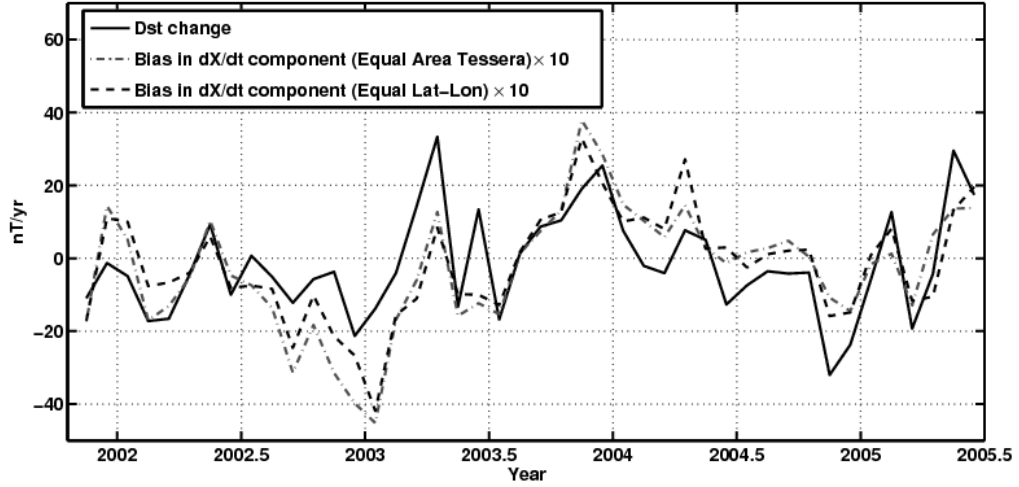


Figure 6. Twelve month difference of mean monthly Dst Index versus the mean bias in the \dot{X} component of Dataset 1 for the equal area tesserae VO grid and the equally-spaced latitude/longitude VO grid. (Note: The biases have been multiplied by 10 to better illustrate the correlation). The correlation is 0.672 and 0.663 respectively (both with a p value of $\sim 10^{-7}$).

5.1 External Field Influences

External effects at satellite altitude come from a large number of phenomena including field aligned currents and ring currents. The Dst index measures magnetic disturbance from external fields, primarily due to ring current activity (Campbell, 2003). Comparison between a nominal average monthly Dst value for 2001–2006 and the mean residual bias in the \dot{X} component of Dataset 1 revealed no obvious correlation. However, as the SV is calculated using data measured twelve months apart, the correct manner of comparison is to compute the difference between the mean monthly Dst values for $month(t - 6)$ and $month(t + 6)$. Figure 6 shows a strong correlation between the annual difference in mean monthly Dst value and the mean bias in the \dot{X} component regardless of which gridding method was used. (As the actual flow model residuals are approximately zero-mean, the \dot{Y} and \dot{Z} component residuals are generally inversely correlated to those of the \dot{X} component). The correlation is 0.673 for the equal area tesserae grid and 0.663 for the equally spaced latitude/longitude grid (both with a p value of $\sim 10^{-7}$, indicating the correlation is significant at greater than the 95% level). The significant correlation between the change in Dst and the two residual means suggests that the residuals contain external field signals.

5.2 Internal Field Influences

Magnetic fields internal to the satellite orbit (in addition to the main and crustal field) can arise from ionospheric currents and auroral/equatorial electrojets, particularly on the sunlit-side of each orbit – increasing globally during solar-disturbed periods. The additional fields would break the assumption of a Laplace potential field in the region surrounding the satellite as measurements are taken.

Examination of the smaller residuals from Dataset 2 (derived from night-side only measurements) compared to Dataset 1 (derived from all-local time measurements) suggests that there is some influence from day-side fields (e.g. Figure 1(g–i) and Figure 3). It was also found, for example, that widening the window of local night-side measurements used from 20.00 – 06.00hrs to 18.00 – 08.00hrs slightly increased the size of the residuals, suggesting that day-side measurements are affected by fields present on the sunlit side of the orbit.

5.3 Influence from the VO method

The method by which each VO is generated through binning and fitting a local potential field to produce an average field measurement over a month is also responsible for some of the residual patterns observed. As the cylindrical bin size (in the latitude/longitude grid) is limited in radius (400km), several effects may arise, including data measurements common to several VO bins (at higher latitudes) and data position bias in any particular month (though this should be removed by the Robust Least-Squares solution). SV calculated using the equal area tesserae grid reduces these effects with the fit of the flows being, on average, better than the those using the evenly-spaced latitude/longitude grid.

The satellite nadir local-time difference also has an effect. As the CHAMP satellite drifts approximately 2.5 hours per month in local time, measurements taken at dawn-dusk configurations are subject to a different ionospheric magnetic field environment to those acquired during local noon-midnight configurations. However, comparison of the mean bias of the \dot{X} component with the mean dayside local time did not reveal any significant correlation. The difference of the median local satellite time (at mid-latitudes) between $month(t+6)$ and $month(t-6)$ is approximately 3.5

hours. Satellite measurements taken at different local times are not sampling the same magnetic field conditions.

The VO dataset created from selected quiet-time Oersted and CHAMP measurements (Dataset 3) has been interpolated from a relatively small number of satellite data points both spatially and temporally. Hence, spatial correlation between measurements is not as strong (though some correlation will exist due to interpolation). The associated residual patterns, shown in Figure 4, do not have any of the features seen in those from Datasets 1 and 2, although the correlation with the change in the Dst index is 0.49 ($p = 10^{-4}$), which suggests that there is some still influence from external fields.

The satellite simulation dataset displays longitudinal banding which, as noted earlier, drifts westward over time. As this dataset is from an essentially ‘noise-free’ simulation using the CHAOS model, it suggests that the binning method applied to generate VO grid and subsequent SV from the satellite data must be partly responsible for the sectorial banding observed.

6 CORRECTION STRATEGIES

Having identified some possible contamination of the VO SV data that might be responsible for the observed biased residuals, we investigate several strategies to reduce these effects. The aim is to produce datasets of purely internal SV which are temporally consistent and spatially un-biased. However, we must at least ensure that there is minimal ‘aliasing’ of undesirable effects into the SV models. These would manifest as unrealistic secular acceleration within the flow models. Olsen & Manda (2008) have indicated that rapid changing flows may occur within the core, but note in the Supplementary Information for their paper that these variations may in part be due to unmodelled external (ionospheric and magnetospheric) sources. They also clearly demonstrate in a previous study (Olsen & Manda, 2007, Figure 6) that the first differences of the external and toroidal field Gauss coefficients (e.g. dq_1^0/dt and dt_1^0/dt) are up to an order of magnitude larger than the coefficients for the internal SV.

	Dataset 1 (Equal Lat-Lon)	Dataset 1 (Equal Area)	Dataset 2 (Equal Lat-Lon)	Dataset 2 (Equal Area)
No correction	0.66	0.67	0.63	0.63
CM4 correction	0.41	0.42	0.10	0.10

Table 1. Correlation between the mean bias of the \dot{X} component of the residuals for each Dataset and the annual Dst difference.

6.1 Removal of fields using the Comprehensive Model

Modelling and removal of external, toroidal and induced magnetic fields at satellite is complex. These magnetic field have not been fully parameterised, nor can they be completely removed (Thomson & Lesur, 2007). However, models of the external and major contributory magnetic fields can be used to correct measured satellite data.

In this study, the Comprehensive Model (CM4) from Sabaka *et al.* (2004) was used to remove external and ionospheric fields from the CHAMP satellite data using the hourly Dst Index and the monthly F10.7 index. The sum of the primary and secondary magnetospheric and ionospheric fields and the toroidal field were subtracted from the individual CHAMP measurements before binning and solving for VO. The resulting residuals from the flow models showed mixed results compared to those observed in Dataset 1, but did not, on average, produce a better fit (using the sum of the absolute values of the residual) than Dataset 2. However, this correction does reduce the correlation between the residual bias and the annual Dst difference. Table 1 shows the correlations between the annual Dst difference and the four VO datasets and two binning methods.

This approach has the largest effect for Dataset 2, where selected ‘night-side’ data are used. However, correcting using CM4 does not improve the fit of the flow to the data, as the size of the residuals remain approximately equal (for an equivalent the solution norm). Figure 7 illustrates the relative fit of the flow models to the data using the sum of the absolute values of the residuals (using the Equal Area tesserae binning method). Dataset 2 without CM4 correction consistently provides the best fit to the data, though for some months (particularly towards the end of the data set), the CM4 corrected datasets are better. Individual comparison of the flow models between the CM4 corrected and uncorrected datasets show strong similarities. It would appear that CM4 removes the external part of the field correctly, but introduces other unwanted signal.

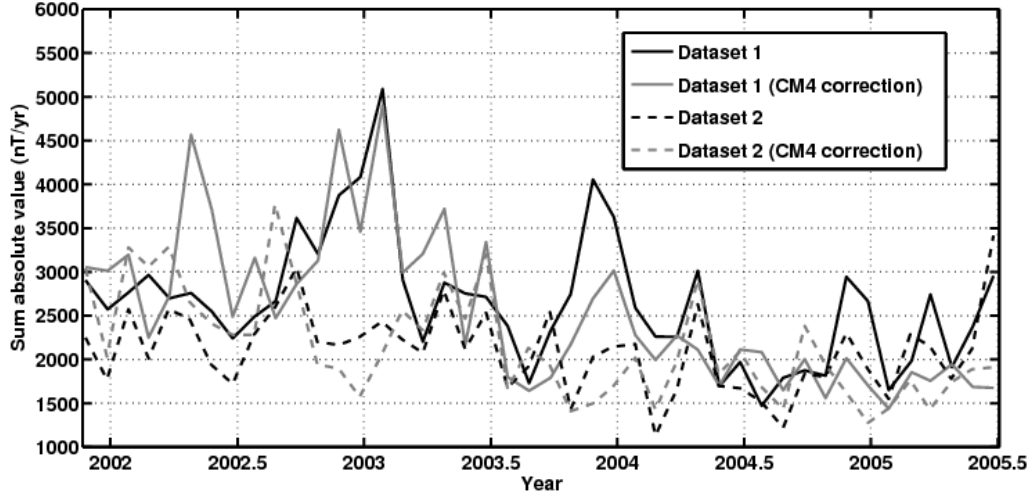


Figure 7. Comparison of the sum of absolute value of the residuals for Datasets 1 and 2 (grid of equal latitude/longitude) when data correction with CM4 is applied. Note the solution norms are approximately similar.

6.2 Smoothing using Steady Flow or B-Splines

Alternative approaches to applying a correction to the satellite data are (a) to calculate steady flows over the specified period, averaging out the changing monthly flows or (b) fit a series of B-splines to the flow coefficients.

Steady flows calculated over the entire dataset period using Datasets 1 and 2, are very consistent, as indicated by their correlation coefficient, which can be expressed as

$$\mathcal{C} = \frac{\sum_{l=1}^{l_{max}} \frac{l(l+1)}{2l+1} \sum_{m=0}^l (s_{l1}^m s_{l2}^m + t_{l1}^m t_{l2}^m)}{\sqrt{\sum_{l=1}^{l_{max}} \frac{l(l+1)}{2l+1} \sum_{m=0}^l (s_{l1}^{m2} + t_{l1}^{m2}) \sum_{l=1}^{l_{max}} \frac{l(l+1)}{2l+1} \sum_{m=0}^l (s_{l2}^{m2} + t_{l2}^{m2})}} \quad (7)$$

where l is the degree, m is the order of the flow coefficients of the spherical harmonic expansion of the toroidal and poloidal scalars t and s ; l_{max} is the maximum degree of the flow solution. Flows models that are similar have a correlation coefficient close to 1. Table 2 shows the correlation coefficients of the various steady flows generated by Datasets 1 and 2 with and without CM4 correction. The values are remarkably consistent (for equivalent solution norms), suggesting that steady flows are removing the finer scale temporal features, producing a smoother flow solution. Note, the monthly residuals to the steady flows reveal patterns similar to those from Dataset 1,

	A	B	C	D
A: Dataset 1: No correction	1	0.91	0.97	0.92
B: Dataset 1: CM4 correction		1	0.91	0.91
C: Dataset 2: No correction			1	0.93
D: Dataset 2: CM4 correction				1

Table 2. Correlation matrix of steady flow coefficients for Datasets 1 and 2 generated from 44 months of SV data.

confirming that particular flow model assumptions are not directly related to or the cause of the residual patterns.

In comparison, fitting the flow coefficients with cubic B-splines can be used to examine temporal changes in the flow. The splines indicate that much of the temporal variation tends to be small. Use of B-splines to fit the flow coefficients would allow the flow velocity to vary slightly over the period in question. By altering the tension within the spline, the amount of SV and secular acceleration can be adjusted. Spline fitting does not assume any particular form for the variation. Experiments indicate that spline coefficients can capture the slowly varying temporal signal, smoothing out the rapid monthly changes. This allows some secular acceleration to be parameterised through the B-splines.

6.3 Spherical Harmonic Analysis of the VO datasets

Applying spherical harmonic analysis to a VO field model will separate it into its internal, external and toroidal parts (Merrill et al., 1996). The internal part of the field should be free of external and toroidal signals. As expected the external part of the field was the most strongly correlated to the annual Dst difference. The SV of each part was calculated and inverted for a flow model. The internal flow models still retained rapid temporal variation, suggesting the some effect remained from the binning and differing sampling conditions. The flow models from the toroidal and external parts of the field represent approximately 3.5% and 0.5% of the power respectively. The external flow model residuals are similar to those observed in Datasets 1 and 2. Examination of the residuals from the internal part show they are more randomly distributed than those from

Dataset	Internal	External	Toroidal
Dataset 1: No correction	0.12 (0.42)	0.64 (3e-6)	0.02 (0.91)
Dataset 1: CM4 correction	-0.11 (0.47)	0.38 (0.01)	-0.01 (0.53)
Dataset 2: No correction	0.01 (0.7)	0.61 (1e-5)	0.12 (0.43)
Dataset 2: CM4 correction	0.04 (0.77)	0.05 (0.74)	0.23 (0.14)

Table 3. Correlation between the mean bias of the \dot{X} component of the residuals for the Internal, External and Toroidal parts of Datasets 1 & 2 and the annual Dst difference. Confidence (p-value) show in brackets.

Datasets 1 and 2, confirming that the external part of the field contains much of the external signal. However, there is still a time varying component in the flow models, suggesting that some external signal remains. This supports the assertion of Olsen & Mandeia (2008) that isolating the internal SV is difficult to achieve. Table 3 shows the correlation of the mean value of the \dot{X} component of the internal, external and toroidal parts of the SV with the Dst Index.

7 CONCLUSION

The results from this study suggest that some non-zero-mean signal remains in the VO. The biased geographic distribution of the residuals and the temporally changing direction of both the flows and the residuals in Figures 1 and 3 support this argument. When viewed in sequence, the flow models generated from the CHAMP vector data (Dataset 1) show rapid variation in direction, strength and structure from month to month. The geographic distribution of the residuals also show continuous variation in component bias (from positive to negative), hemispherical bias, sectorial pattern and magnitude of bias.

There is a small improvement in the fit of the flows to the data when the night-side only vector data are used to create a VO dataset (Dataset 2). A similar improvement can be seen when each satellite datum is corrected using a CM4 model to remove expected external and internal (to the satellite) fields prior to binning. This points to ionospheric and day-side current systems as another source for contamination. In contrast, the weak residuals from the selected quiet-time Oersted-CHAMP data (Dataset 3) indicates that contamination of the VO data is much less, though still

present indicating signals external to the satellite orbit may be one source of such contamination (for our purposes).

Another potential source of non-zero mean error is the method of generating the VO dataset. The CHAMP satellite precesses approximately 2.5 hours per month in local time. As the data used to generate the VO are not from all local times, but rather a small subset of day/night local times, this has the effect of *not* averaging out diurnal effects. For example, in a month where the local time is noon on the day side and midnight on the night side, a significant bias must be present due to currents internal to the satellite orbit. As noted in Equation (3) to calculate the annual SV for a particular month the VO value for six months prior is subtracted from the VO value six months ahead. Typically, the difference in the satellite nadir local times 12 months apart is between 3-5 hours. For example, a VO with a predominantly noon local time subtracted from a VO with predominantly morning local time will sense different ionospheric-related fields. A grid with equal latitude/longitude spacing, where bins overlap near the poles and have gaps between them at the low latitudes, rather than equal area tessera was found to accentuate certain patterns, such as sectorial banding and predominance of large residuals at the polar regions. The results from the synthetic dataset support this conclusion.

Correction of the satellite data for fields external to the Earth prior to solving for each VO did produce a slight improvement in the fit of the flow models to the data but was inconsistent, with some months being better and others worse than non-corrected data. It is not clear why this happens, but suggests despite best efforts to parameterise and remove external fields, some small part remains in the monthly internal SV models.

Steady flow models generated from the entire set of SV data of 44 months produce very consistent flow regimes, while B-spline fit to the flow coefficients can also smooth the variation from month to month. Examination of the internal, external and toroidal parts of the field partitioned most of the influence from external sources into the external part of the field, as expected. However, the internal component still retained a temporally varying signal, most likely related to some unmodelled external source and, perhaps, the binning approach adopted.

In conclusion, signals from a number of sources have been identified in the field models de-

rived from employing the VO method. Some of the effects from these sources can be removed or ameliorated, through the selective use of data, external field modelling and alternative binning approach. However, additional smoothing in the form of steady flow or B-spline fitting is required to produce realistic secular variation and flow modelling. Using the equal-area tessera gridding method, with local night side only data selection (as in Dataset 2), best isolates the internal SV and reduces the influence from other sources. However, we must still argue that rapidly changing flows appear to derive from unmodelled sources external to main field SV.

ACKNOWLEDGMENTS

We wish to thank Nils Olsen for his advice and for code and for providing certain CHAMP data and the CHAOS model. We also thank Alan Thomson for the provision of selected Oersted data. The CHAMP data used in this study were supplied by GFZ Potsdam. This research is part of the NERC GEOSPACE programme, funded under grant NER/O/S/2003/00674. CDB is funded under NERC studentship award NER/S/J/2005/13496.

REFERENCES

- Alfvén, H., 1942. Existence of electromagnetic-hydrodynamic waves, *Nature*, **150**, 405–406.
- Amit, H. & Olson, P., 2004. Helical core flow from geomagnetic secular variation, *Phys. Earth Planet. Int.*, **147**, 1–25.
- Amit, H., Olson, P., & Christensen, U., 2007. Tests of core flow imaging methods with numerical dynamos, *Geophys. J. Int.*, **168**, 27–39.
- Backus, G. E., 1968. Kinematics of geomagnetic secular variation in a perfectly conducting core, *Philos. Trans. R. Soc. Lond. Ser A*, **263**, 239–266.
- Beggan, C. & Whaler, K., 2008. Core flow modelling assumptions, *Phys. Earth Plan. Int.*, **167**, 217–222.
- Bloxham, J., 1988. *The determination of fluid flow at the core surface from geomagnetic observations*, vol. Mathematical Geophysics, chap. 9, pp. 189–208, D. Reidel Publishing Company.
- Bloxham, J., 1989. Simple models of fluid flow at the core surface derived from geomagnetic field models, *Geophys. J. Int.*, **99**(1), 173–182.
- Bloxham, J., Gubbins, D., & Jackson, A., 1989. Geomagnetic secular variation, *Philos. Trans. R. Soc. Lond.*, **329**(1606), 415–502.
- Campbell, W., 2003. *Introduction to Geomagnetic Fields*, Cambridge University Press.

- Gubbins, D., 1983. Geomagnetic field analysis - I. Stochastic inversion, *Geophys. J. R. Astr. Soc.*, **73**(3), 641–652.
- Gubbins, D. & Kelly, P., 1996. A difficulty with using the frozen flux hypothesis to find steady core motions, *Geophys. Res. Lett.*, **23**(14), 1825–1828.
- Hills, R., 1979. *Convection in the Earth's mantle due to viscous shear at the core-mantle interface and due to large-scale buoyancy*, Ph.D. thesis, N.M. State Univ., Las Cruces.
- Holme, R. & Olsen, N., 2006. Core surface flow modelling from high-resolution secular variation, *Geophys. J. Int.*, **166**, 518–528.
- Hulot, G., Eymin, C., Langlais, B., Manda, M., & Olsen, N., 2002. Small-scale structure of the geodynamo inferred from Oersted and Magsat satellite data, *Nature*, **416**, 620–623.
- Jackson, A., 1997. Time-dependency of tangentially geostrophic core surface motions, *Phys. Earth Plan. Int.*, **103**, 293–311.
- Kahle, A., Vestine, E., & Ball, R., 1967. Estimated surface motions of the Earth's core, *J. Geophys. Res.*, **72**, 1095–1108.
- Le Mouél, J., 1984. Outer-core geostrophic flow and secular variation of Earth's geomagnetic field, *Nature*, **311**, 734 – 735.
- Leopardi, P., 2006. A partition of the unit sphere into regions of equal area and small diameter, *Electronic Transactions on Numerical Analysis*, **25**, 309–327.
- Love, J., 1999. A critique of frozen-flux inverse modelling of a nearly steady geodynamo, *Geophys. J. Int.*, **138**, 353–365.
- Manda, M. & Olsen, N., 2006. A new approach to directly determine the secular variation from magnetic satellite observations, *Geophys. Res. Lett.*, **33**(15), L15306.
- Merrill, R., McElhinny, M., & McFadden, P., 1996. *The Magnetic Field of the Earth: Paleomagnetism, the Core and the Deep Mantle*, vol. 63 of **International Geophysics Series**, Academic Press, New York.
- Neubert, T., Manda, M., Hulot, G., von Frese, M., Primdahl, F., Jurgensen, J. L., Friis-Christensen, E., Stauning, P., Olsen, N., & Risbo, T., 2001. Oersted satellite captures high-precision geomagnetic field data, *Eos Trans. AGU*, **82**(7), 87–88.
- Olsen, N. & Manda, M., 2007. Investigation of a secular variation impulse using satellite data: The 2003 geomagnetic jerk, *Earth Planet. Sci. Lett.*, **255**, 94–105.
- Olsen, N. & Manda, M., 2008. Rapidly changing flows in the Earth's core, *Nature Geoscience*, **1**, 390–394.
- Olsen, N., Luhr, H., Sabaka, T., Manda, M., Rother, M., & Toffner-Clausen, L., 2006. CHAOS: a model of the Earth's magnetic field derived from CHAMP, Oersted, and SAC-C magnetic satellite data, *Geophys. J. Int.*, **166**, 67–75.
- Rau, S., Christensen, U., Jackson, A., & Wicht, J., 2000. Core flow inversion tested with numerical dynamo models, *Geophys. J. Int.*, **141**, 485–497.

- Reigber, C., Luhr, H., & Schwintzer, P., 2002. CHAMP mission status, *Adv. Space Res.*, **30**, 129–134.
- Roberts, P. & Scott, S., 1965. On the analysis of the secular variation. 1. A hydromagnetic constraint: Theory, *J. Geomag. Geoelec.*, **17**, 137–151.
- Sabaka, T., Olsen, N., & Purucker, M., 2004. Extending comprehensive models of the Earth's magnetic field with Oersted and CHAMP data, *Geophys. J. Int.*, **159**, 521–547.
- Thomson, A. & Lesur, V., 2007. An improved geomagnetic data selection algorithm for global geomagnetic field modelling, *Geophys. J. Int.*, **169**, 951–963.
- Voorhies, C. & Backus, G., 1985. Steady flows at the top of the core from geomagnetic field models: The steady motion theorem, *Geophys. Astrophys. Fluid Dynam.*, **32**, 163–173.
- Walker, M. & Jackson, A., 2000. Robust modelling of the Earth's magnetic field, *Geophys. J. Int.*, **143-3**, 799–808.
- Waler, K., 1980. Does the whole of the Earth's core convect?, *Nature*, **287**, 528–530.
- Waler, K. A., 1986. Geomagnetic evidence for fluid upwelling at the core-mantle boundary, *Geophys. J. R. Astr. Soc.*, **86**, 563–588.
- Waler, K. A., 2007. *Encyclopedia of Geomagnetism and Paleomagnetism*, chap. Core Motions, pp. 84–89, Springer, Dordrecht.